THE JOURNAL OF PHYSICAL CHEMISTRY A

Article

pubs.acs.org/JPCA

5-Methylhydantoin: From Isolated Molecules in a Low-Temperature Argon Matrix to Solid State Polymorphs Characterization

B. A. Nogueira,*[,†] G. O. Ildiz,*[,†,‡] J. Canotilho,[§] M. E. S. Eusébio,[†] M. S. C. Henriques,[∥] J. A. Paixão,[∥] and R. Fausto[†]

[†]CQC, Department of Chemistry, University of Coimbra, P-3004-535 Coimbra, Portugal

[‡]Faculty of Sciences and Letters, Department of Physics, Istanbul Kültür University, Ataköy Campus, Bakirköy 34156, Istanbul, Turkey

[§]Faculty of Pharmacy, University of Coimbra, Coimbra, Portugal

[∥]CFisUC, Department of Physics, University of Coimbra, P-3004-516 Coimbra, Portugal

Supporting Information

ABSTRACT: The molecular structure, vibrational spectra and photochemistry of 5-methylhydantoin ($C_4H_6N_2O_2$; 5-MH) were studied by matrix isolation infrared spectroscopy and theoretical calculations at the DFT(B3LYP)/6-311++G(d,p) theory level. The natural bond orbital (NBO) analysis approach was used to study in detail the electronic structure of the minimum energy structure of 5-MH, namely the specific characteristics of the σ and π electronic systems of the molecule and the stabilizing orbital interactions. UV irradiation of 5-MH isolated in argon matrix resulted in its photofragmentation through a single photochemical pathway, yielding isocyanic acid, ethanimine, and carbon monoxide, thus following a pattern already observed before for the parent hydantoin and 1-methylhydantoin molecules. The investigation of the thermal properties of 5-MH was undertaken by differential scanning calorimetry (DSC), polarized light thermal microscopy (PLTM) and Raman spectroscopy. Four different polymorphs of 5-MH were identified. The crystal structure of one of the polymorphs, for which it was possible to grow up suitable crystals, was determined by X-ray diffraction (XRD). Two of the additional polymorphs were characterized by powder XRD, which confirmed the molecules pack in different crystallographic arrangements.

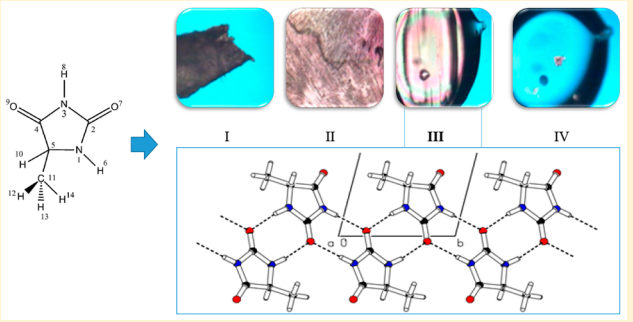

1. INTRODUCTION

Hydantoins have remarkable interest from the chemical and biological perspectives,[1−7] and they have also been shown to receive widespread applications in medicine, agriculture, and the chemical industry.[8−15] They have been clinically used as antiepileptic and antibacterial drugs[12,13] and for cancer and AIDS treatments[8−11] and are also used as herbicides and fungicides.[14,15] Among the hydantoins, the 5-monosubstituted derivatives are particularly interesting from a structural viewpoint because they exhibit optical isomerism. In spite of their practical relevance, hydantoins have not yet been investigated in much detail in relation to their molecular properties, their ability to generate different polymorphic varieties in the solid state, and their photochemistry.

The parent hydantoin and 1-methylhydantoin (1-MH) were previously studied by our group, both in their monomeric forms isolated in cryogenic inert matrices and in the neat solid phases.[16−18] The structures and electron distribution characteristics of these two molecules were investigated by quantum chemical methods, and their vibrational properties and photochemistry in low-temperature argon matrices were reported.[16−18] In addition, we have addressed the study of polymorphism in these compounds. The structural analysis showed that both compounds have C_s symmetry, with a planar ring. After UV (λ = 230 nm) irradiation, matrix-isolated hydantoin undergoes ring photocleavage leading to production of isocyanic acid, carbon monoxide and methylenimine,[17] while 1-MH gives rise to isocyanic acid, carbon monoxide, methylenimine, and *N*-methyl methylenimine.[18] According to the observations, the 230 nm induced photolysis of matrix-isolated 1-MH occurs via two different pathways, which lead to fragmentation to (a) OCNH + CO + $H_2C{=}NCH_3$ and (b) 2CO + $2H_2C{=}NH$. Pathway a was proposed to occur through a concerted mechanism, where the weak C2−N3 and C4−C5 bonds are cleaved, yielding an isocyanic acid molecule and triggering the cleavage of the stronger N1−C2 bond with production of CO and *N*-methyl methylenimine,[18] and follows closely the previously reported photofragmentation of the parent hydantoin molecule isolated in an argon matrix and subjected to identical experimental conditions.[17] Pathway b, on

Received: May 24, 2017
Revised: June 21, 2017
Published: June 22, 2017

DOI: 10.1021/acs.jpca.7b05030
J. Phys. Chem. A 2017, 121, 5267−5279

the other hand, is most probably a more complex process, where extrusion of two molecules of CO should lead to formation of the NH radical, which then reacts with the remaining fragment (CH_2NCH_3) to produce two methylenimine molecules.[18]

In this work, 5-methylhydantoin (5-MH; Scheme 1) has been chosen as target for investigation. This compound is used

Scheme 1. 5-Methylhydantoin Molecule with the Adopted Atom Numbering

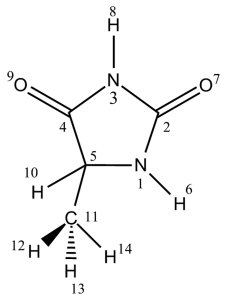

in the synthesis of several pharmaceutical drugs,[19] and is the smallest 5-monoalkyl-substituted hydantoin. The molecular structure of 5-MH and its electron distribution were studied by quantum chemical methods, and the infrared spectrum of the 5-MH molecules isolated in an argon matrix (10 K) was obtained and interpreted. In addition, the unimolecular photochemistry exhibited by matrix-isolated 5-MH was also investigated. As described in details below, it was found that upon broadband UV irradiation (λ > 220 nm) 5-MH undergoes photofragmentation through a single pathway, yielding as final products isocyanic acid, ethanimine and carbon monoxide, thus following closely the same pattern of reactivity of the parent hydantoin (and also pathway a of 1-MH; see above).[17,18] Finally, neat crystalline 5-MH was investigated by Raman spectroscopy, X-ray diffraction, differential scanning calorimetry, and polarized light thermomicroscopy, which allowed identification of four different 5-MH polymorphs. The crystal structure of one of these crystalline varieties was successfully solved and is reported here for the first time and discussed in terms of its determining dominant intermolecular interactions.

2. EXPERIMENTAL AND COMPUTATIONAL METHODS

5-Methylhydantoin was purchased from Sigma-Aldrich (98% purity) and used without further purification. For preparation of the cryogenic matrices, 5-MH was sublimated using a specially designed furnace mounted inside the cryostat, and the vapor codeposited with argon gas (Air Liquide, N60) onto a CsI window connected to the cold (10 K) tip of the cryostat (APD Cryogenics closed-cycle helium refrigeration system, with a DE-202A expander). The temperature of the CsI window was measured by a silicon diode sensor, connected to a digital temperature controller (Scientific Instruments, model 9650−1), with an accuracy of 0.1 deg.

The matrix-isolated 5-MH was irradiated through a quartz window in the range 230−222 nm, using a tunable UV laser/MOPO system (repetition rate = 10 Hz, pulse energy 10 mJ, duration = 10 ns) as radiation source, and also with broadband UV light produced by a 500 W Hg(Xe) lamp (Newport, Oriel Instruments) fitted with a 8 cm water filter to avoid the heating of the sample.

The infrared spectra were recorded, in the 4000−400 cm^{-1} range, using a Nicolet 6700 FTIR spectrometer, equipped with a Ge/KBr beam splitter and a deuterated triglycine sulfate (DTGS) detector, with 0.5 cm^{-1} spectral resolution for the matrix isolation studies and 1 cm^{-1} for the studies on the neat solid compound.

Raman spectra of the polymorphs were obtained using a Horiba LabRam HR Evolution micro-Raman system, with excitation at 632.8 nm from a He−Ne laser, spectral resolution 1.5 cm^{-1}, 100× magnification objective (spot size 0.85 μm), acquisition time of 60 s, 10 accumulations, and laser power ∼17 mW. Calibration was done using the characteristic Si wafer band. The wavenumber accuracy is better than 0.5 cm^{-1} in the spectral region of interest.

Differential scanning calorimetry (DSC) measurements were performed on a PerkinElmer Pyris-1 power compensation calorimeter, with an ethylene glycol-water (1:1 v/v) cooling mixture at −25 °C and a 20 mL min^{-1} nitrogen purge flow. Hermetically sealed aluminum pans were used in these studies (samples weight between 1.2 and 2.0 mg), and an empty pan was used as reference. Indium (PerkinElmer, 99.99%, T_{fus} = 156.60 °C) and biphenyl (CRM LGC, T_{fus} = 68.93 °C ± 0.03 °C)[20] were used in the temperature and enthalpy calibrations. In these experiments, the samples were scanned from 25 to 155 °C at a scan rate of 10 °C min^{-1}.

Images of the compound within the range of temperature of the DSC experiments were obtained with polarized light thermal microscopy (PLTM) by combined used of polarized light and wave compensators, with magnification power of 200x, a hot stage DSC600 Linkam system attached to a Leica DMRB microscope, and to a Sony CCD-IRIS/RGB video camera. The analysis of the images was done with the Linkam Real Time Video Measurement System software.

Melting cooling/heating cycles performed by DSC and/or PLTM and crystallization from different solvents were used for polymorph screening. In the crystallization experiments 5-MH (ca. 35 mg) solutions in dichloromethane, 1,4-dioxane, tetrahydrofuran (THF), acetone, water, methanol and ethanol (with volumes of 4 to 20 mL) were prepared and allowed to evaporate at room temperature. The polymorphs were further evaluated by IR, Raman, and X-ray diffraction.

Single crystal X-ray diffraction data for polymorph III (obtained by recrystallization from ethanol) were collected on a Bruker APEXII diffractometer (Mo Kα radiation, graphite monochromator, λ = 0.71073 Å) using φ and ω scans. Data integration and scaling were performed with the SAINT suite of programs[21] and SADABS[21] was used for an empirical absorption collection based on a measurement of a large set of redundant reflections. The structure was solved by direct methods using SHELXT-2014/5[22] and full-matrix least-squares refinement of the structural model was performed by SHELXL-2016/6.[23] All non-H atoms were refined anisotropically. H atoms were placed at calculated idealized positions and refined as riding using SHELXL-2016/6 default values, except for those of the N−H groups that where fully refined isotropically. A summary of the data collection and refinement details is given in Table S1 (Supporting Information). Crystallographic figures and tables were produced using PLATON.[24] A CIF file containing supplementary crystallographic data was deposited at the Cambridge Crystallographic Data Centre with reference CCDC 1527432.

Powder X-ray diffraction data were collected form polymorphs I and II on a Bruker D8 Advance diffractometer using

DOI: 10.1021/acs.jpca.7b05030
J. Phys. Chem. A 2017, 121, 5267−5279

Cu Kα radiation, λ = 1.54178 Å. A Ni foil was used as filter for suppression of the Kβ line. A 1D LynxEye Silicon Drift detector with 192 pixels, covering a 2θ angular range of ∼3° was used. The patterns were collected in Bragg−Brentano geometry, in continuous scan mode, from 5 to 90° with an angular step of 0.01° and an effective counting time per angular step of 96 s. A divergence slit of 0.2° was used for primary beam conditioning and a knife edge was mounted close to the sample to reduce air scattering at low angles. A low-background silicon sample holder was used.

All quantum chemical calculations were performed with the Gaussian 09 program, at the DFT(B3LYP) theory level,[25−27] using the 6-311++G(d,p) basis set.[28] For the interpretation of the experimental spectra, vibrational frequencies and intensities were also calculated at the same theory level. The computed harmonic frequencies were scaled by a factor of 0.980, below 3400 cm^{-1}, and by 0.957, above 3400 cm^{-1}, to correct them for the effects of basis set limitations and anharmonicity. Normal coordinate analysis was done using a locally modified version of the program BALGA.[29] The internal symmetry coordinates used in the analysis of normal modes of 5-MH are given in Table S2 (Supporting Information). Natural bond orbital (NBO) analysis was done using NBO (version 3.1), as implemented in Gaussian 09.

3. RESULTS AND DISCUSSION

3.1. Geometry of the 5-MH Molecule. According to the performed calculations (geometrical parameters are shown in Table S3; Supporting Information), the 5-MH molecule has C_1 symmetry (see Scheme 1), with a quasi-planar ring.

The most relevant geometric features shown by the 5-MH molecule closely follow those described before for the parent hydantoin and 1-MH.[17,18] The bond length of the carbonyl group C2═O7 (1.208 Å), which is bonded to two nitrogen atoms, is longer than that of the carbonyl group C4═O9 (1.207 Å) that is connected to a single nitrogen atom, in consonance with the expected larger total π electron delocalization from the nitrogen atoms to O7, compared to O9. The ring C_{sp2}−N bond lengths follow the order C2−N3 > C4−N3 > C2−N1 (1.412, 1.378, 1.369 Å, respectively), pointing out to a maximum N-to-O electron delocalization within the fragment N1−C2═O7, i.e., when the nitrogen atom donates electron charge only to one oxygen atom. On the other hand, the minimum N-to-O electron charge donation occurs within the N3−C2═O7 fragment, because the N3 atom donates electron charge to both O7 and O9, and, since O7 has another donor (N1), N3 donates electron charge preferably to O9. The C4−C5 bond length (1.539 Å) is considerably longer than the typical C_{sp3}−C_{sp2} length (∼1.50 Å),[30] indicating that the methyl substituent bonded to the C5 atom reduces the π delocalization in this part of the molecule.

Following the trend already noticed for the parent hydantoin and 1-MH,[17,18] the internal angles of the ring with a nitrogen atom in the apex (C4−N3−C2 and C5−N1−C2) are much larger (around 113°) than those with carbon atoms in the apex (N1−C2−C3, N1−C5−C4 and N3−C4−C5: ∼101−106°), suggesting relatively different s−p compositions of the hybrid orbitals of the N and C atoms used to make the ring bonds (we will return to this point later).

As mentioned, on the whole the overall geometry of 5-MH is similar to that of parent hydantoin and 1-MH, except in what concerns the geometrical features directly related to the C5 atom to which the methyl substituent is bonded: the lengths of the N1−C5, C4−C5 and C5−H10 bonds are longer in 5-MH than in hydantoin and 1-MH (1.459, 1.539 and 1.097 Å in 5-MH vs 1.451, 1.534 and 1.094 Å, and 1.451, 1.531 and 1.096 Å

Table 1. Natural Bond Orbital (NBO) Atomic Charges for 5-MH, Obtained from the B3LYP/6-3111++G(d,p) Calculations[a]

	NBO charges		
atom[b]	total	σ	π
N1	−0.661	−0.948	0.287
C2	0.809	0.637	0.172
N3	−0.656	−1.010	0.354
C4	0.689	0.484	0.205
C5	−0.095	0.082	−0.176
H6	0.408	–	–
O7	−0.610	−0.078	−0.532
H8	0.421	–	–
O9	−0.581	−0.098	−0.483
H10	0.214	–	–
C11	−0.578	−0.417	−0.160
H12	0.205	–	–
H13	0.225	–	–
H14	0.210	–	–

[a]Charges in units of electron; e = 1.60217646 × 10^{-19} C). [b]See Scheme 1 for atom numbering.

Scheme 2. (I) Dominant Canonic Form of 5-MH and (II, III, and IV) Mesomeric Structures Assuming Delocalization of π Electrons in the NCO Moieties of the Molecule

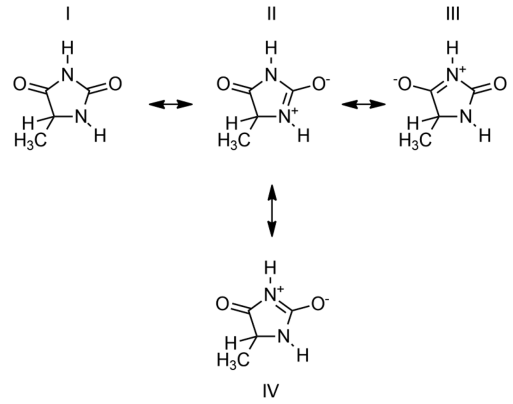

Table 2. Stabilization Energies for Selected NBO Pairs as Given by Second Order Perturbation Theory Analysis of the Fock Matrix in the NBO Basis for 5-MH Obtained from the B3LYP/6-311++G(d,p) Calculations[a]

pair name	donor NBO	acceptor NBO	$-E(2)$ (kcal mol^{-1})
A	LP (N1)	π* (C2−O7)	57.88
B	LP (N3)	π* (C2−O7)	47.70
C	LP (N3)	π* (C4−O9)	54.65
D	LP2 (O7)	σ* (N1−C2)	24.74
E	LP2 (O7)	σ* (C2−N3)	28.49
F	LP2 (O9)	σ* (N3−C4)	27.36
G	LP2 (O9)	σ* (C4−C5)	21.76
H	LP1 (O7)	RY* (C2)	18.57
I	LP1 (O9)	RY* (C4)	18.21

[a]See atom numbering in Scheme 1. LP, lone electron pair orbital. RY, Rydberg type orbital.

DOI: 10.1021/acs.jpca.7b05030
J. Phys. Chem. A 2017, 121, 5267−5279

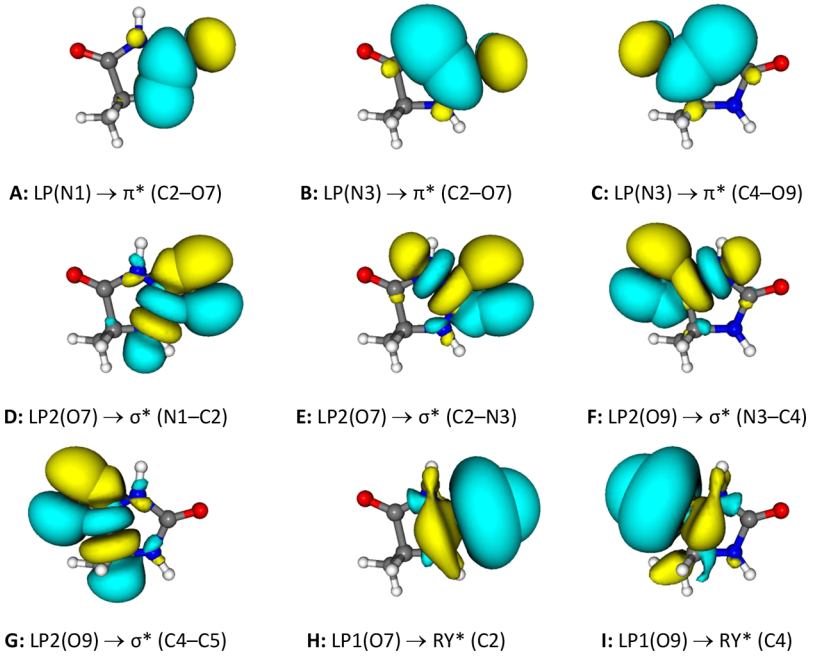

Figure 1. Electron density surfaces of selected NBOs of 5MH calculated at the DFT(B3LYP)/6-311++G(d,p) level of theory, showing the dominant orbital interactions. Isovalues of the electron densities are equal to 0.02 *e*. Yellow and blue colors correspond to negative and positive wave function signs, respectively. Color codes for atoms: red, O; gray, C; white, H; blue, N.

for hydantoin and 1-MH, respectively),[17,18] the C5−N1−H6 angle is larger in 5-MH than in hydantoin (124.8° vs 123.8°),[17] and the N1−C5−C4 is smaller in 5-MH compared with the two other molecules (101.6° in 5-MH vs 102.4° and 103.3°, in hydantoin and 1-MH, respectively). All these structural trends point to a reduction of the π delocalization in the ring around the C5 atom and to a higher sp^3 character of this atom in 5-MH compared with the other molecules.

3.2. Natural Bond Orbital (NBO) Analysis. The NBO analysis carried out on 5-MH allowed to further our understanding on its fundamental structural features, and also extracting some relevant conclusions regarding its chemical reactivity. It is particularly successful to get across the specific characteristics of the σ and π electronic systems of the molecule.

The natural bond orbital atomic charges are shown in Table 1. Both nitrogen atoms have negative total charge, as we could expect because these atoms are more electronegative than the carbon atoms to which they are bonded. Analogously, carbon atoms C2 and C4, which are connected to more electronegative nitrogen and oxygen atoms, have positive total charges, contrasting with C5 and C11 carbon atoms that show a negative total charge because they are bonded to hydrogen atoms. The atom C11 is connected to 3 hydrogen atoms and, for that reason, it is more negative than C5, which is bonded only to one hydrogen atom. The oxygen atoms O7 and O9, being the most electronegative atoms in the molecule, have considerably negative total charges (−0.610 and −0.578 *e*, respectively).

The total NBO charges do not provide more than a very general (and simplified) picture of the electronic structure of the molecule. Here we present the NBO charges partition in terms of the electronic σ and π systems. This analysis brings to light some considerably more interesting details of the electron distribution in the molecule.

The first thing to note is that, although the nitrogen atoms have a negative total charge, they present a positive π charge, in agreement with the mesomeric structures **II**, **III**, and **IV** depicted in Scheme 2. The N3 atom has a π charge that is more positive than N1, in agreement with the fact that N3 shows a positive charge in mesomeric structures **III** and **IV** (see Scheme 2), while N1 only shows a positive charge in mesomeric structure **II**. A similar reasoning can be applied to understand the relative values of the π charges of the two oxygen atoms connected to the ring. Since O7 shows a negative charge in two mesomeric structures (**II** and **IV**) and O9 is negatively charged only in mesomeric structure **III**, the O7 atom has a more negative π charge than O9.

Another remarkable feature concerns the σ charges of the two oxygen atoms, since they are considerably less negative than the corresponding π charges and have opposite relative values (the O9 σ charge is more negative than the O7 σ charge; see Table 1). This shows that, in comparison with C4═O9, the larger C2═O7 π bond polarization toward the oxygen atom leads to reduce the trend for the associated σ bond to be polarized in the same direction. The O7 atom is, nevertheless, more negatively charged than O9, in result of its highly polarized π bond through mesomerism. Indeed, these results are in full agreement with the structural results discussed in the previous section (in particular with the relative C2═O7 and C4═O9 bond lengths), which have indicated a larger π electron delocalization from the nitrogen atoms to O7, compared to O9.

The relative values of the π charges of the nitrogen atoms are also in agreement with the lengths of the C_{sp2}−N bonds. As discussed above, the structural results point to a maximum N-to-O electron delocalization in the N1−C2═O7 fragment. Accordingly, the positive π charge of the N1 atom (+0.287 *e*), resulting essentially from the π delocalization to O7 (see Scheme 2), is considerably larger than half of the positive

DOI: 10.1021/acs.jpca.7b05030
J. Phys. Chem. A 2017, 121, 5267−5279

Table 3. Selected NBOs for 5-MH Obtained from the B3LYP/6-311++G(d,p) Calculations

bond orbital[a] T(A−B)	occupancy[b] (e)	coefficients (%)[c] A	B	description[d]
σ(N1−C2)	1.987 39	61.75	38.25	0.7858 $sp^{1.90}$ + 0.6185 $sp^{2.02}$
σ(N1−C5)	1.984 14	61.66	38.34	0.7852 $sp^{1.91}$ + 0.6192 $sp^{3.46}$
σ(N1−H6)	1.987 82	70.92	29.08	0.8422 $sp^{2.34}$ + 0.5392 s
σ(C2−N3)	1.984 36	37.12	62.88	0.6093 $sp^{2.31}$ + 0.7929 $sp^{2.00}$
σ(C2═O7)	1.994 78	36.35	63.65	0.6029 $sp^{1.73}$ + 0.7978 $sp^{1.49}$
π(C2═O7)	1.991 99	28.65	71.35	0.5352 p + 0.8447 p
σ(N3−C4)	1.988 84	62.85	37.15	0.7928 $sp^{1.79}$ + 0.6095 $sp^{2.27}$
σ(N3−H8)	1.988 02	71.64	28.36	0.8464 $sp^{2.26}$ + 0.5326 s
σ(C4−C5)	1.968 15	48.15	51.85	0.6939 $sp^{1.90}$ 0.7201 $sp^{3.10}$
σ(C4═O9)	1.995 63	35.59	64.41	0.5965 $sp^{1.88}$ + 0.8026 $sp^{1.42}$
π(C4═O9)	1.991 22	30.58	69.42	0.5530 p + 0.8332 p
σ(C5−H10)	1.962 20	60.93	39.07	0.7806 $sp^{3.32}$ + 0.6251 s
σ(C5−C11)	1.976 28	52.30	47.70	0.7232 $sp^{2.30}$ + 0.6906 $sp^{2.54}$
σ(C11−H12)	1.986 66	60.21	39.79	0.7760 $sp^{3.21}$ + 0.6308 s
σ(C11−H13)	1.988 72	60.56	39.44	0.7782 $sp^{3.14}$ + 0.6280 s
σ(C11−H14)	1.983 47	61.18	38.82	0.7822 $sp^{3.17}$ + 0.6231 s
Cr(N1)	1.999 34			s
Cr(C2)	1.999 46			s
Cr(N3)	1.999 27			s
Cr(C4)	1.999 37			s
Cr(C5)	1.999 19			s
Cr(O7)	1.999 74			s
Cr(O9)	1.999 74			s
Cr(C11)	1.999 30			s
LP(N1)	1.748 34			p
LP(N3)	1.659 63			p
LP1(O7)	1.978 78			$sp^{0.67}$
LP2(O7)	1.834 49			p
LP1(O9)	1.978 81			$sp^{0.71}$
LP2(O9)	1.850 57			p
Ry*(C2)	0.015 67			$sp^{11.06}d^{0.06}$
Ry*(C4)	0.016 39			$sp^{6.09}d^{0.02}$
σ*(N1−C2)	0.076 99	38.25	61.75	0.6185 $sp^{1.90}$ − 0.7858 $sp^{2.02}$
σ*(N1−C5)	0.025 25	38.34	61.66	0.6192 $sp^{1.91}$ − 0.7852 $sp^{3.46}$
σ*(N1−H6)	0.015 32	29.08	70.92	0.5392 $sp^{2.34}$ − 0.8422 s
σ*(C2−N3)	0.091 84	62.88	37.12	0.7929 $sp^{2.31}$ − 0.6093 sp^{2}
σ*(C2═O7)	0.010 99	63.65	36.35	0.7978 $sp^{1.73}$ − 0.6029 $sp^{1.49}$
π*(C2═O7)	0.342 99	71.35	28.65	0.8447 p−0.5352 p
σ*(N3−C4)	0.080 87	37.15	62.85	0.6095 $sp^{1.79}$ − 0.7928 $sp^{2.27}$
σ*(N3−H8)	0.015 46	28.36	71.64	0.5326 $sp^{2.26}$ − 0.8464 s
σ*(C4−C5)	0.079 47	51.85	48.15	0.7201 $sp^{1.90}$ − 0.6939 $sp^{3.10}$
σ*(C4═O9)	0.011 21	64.41	35.59	0.8026 $sp^{1.88}$ − 0.5965* $sp^{1.42}$
π*(C4═O9)	0.243 70	69.42	30.58	0.8332 p−0.5530 p
σ*(C5−H10)	0.028 48	39.07	60.93	0.6251 $sp^{3.32}$ − 0.7806 s
σ*(C5−C11)	0.017 12	47.70	52.30	0.6906 $sp^{2.30}$ − 0.7232 $sp^{2.54}$
σ*(C11−H12)	0.005 48	39.79	60.21	0.6308 $sp^{3.21}$ − 0.7760 s
σ*(C11−H13)	0.006 89	39.44	60.56	0.6280 $sp^{3.14}$ − 0.7782 s
σ*(C11−H14)	0.005 08	38.82	61.18	0.6231 $sp^{3.17}$ − 0.7822 s

[a]See atom numbering in Scheme 1. Cr, core orbital; LP, lone electron pair orbital; Ry*, Rydberg orbital. [b]Occupancy is given with an exaggerated accuracy, as in the Gaussian output file. [c]The A and B values correspond to the contributions of the atomic orbitals of the two atoms forming a bond (by order of appearance in the corresponding entry in the first column) for the NBO orbitals, extracted from the polarization coefficients given in the description of the NBO orbitals. [d]The presented description is made in the space of the input atomic orbitals, as given by 6-311++G(d,p) basis set used in the calculations.

charge of the atom N3 (+0.177 e), which donates π electron charge to both O7 and O9 oxygen atoms.

Table 2 and Figure 1 present the most relevant NBO interactions, which also show the relative relevance of the mesomerism within the different NCO fragments of the 5-MH molecule, together with other important intramolecular interactions. The orbital interaction energies, $-E(2)$, between filled and empty NBOs (including non-Lewis extra-valence Rydberg orbitals), were obtained from the second-order perturbation approach:

DOI: 10.1021/acs.jpca.7b05030
J. Phys. Chem. A 2017, 121, 5267−5279

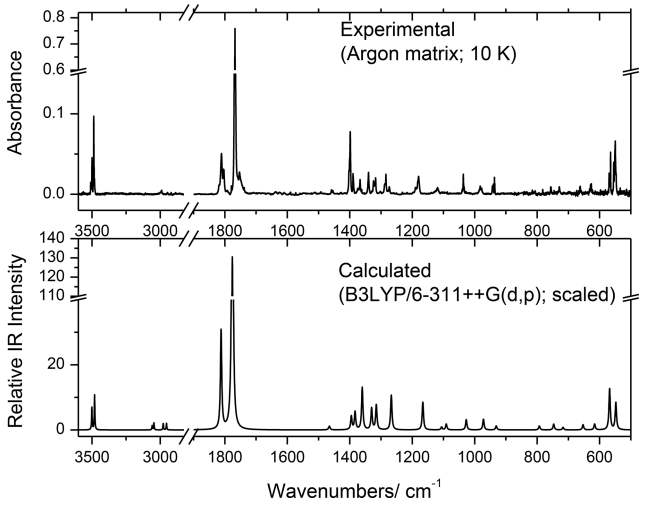

Figure 2. Experimental infrared spectrum of monomeric 5-MH isolated in an argon matrix at 10 K (top) and simulated spectrum of 5-MH monomer using Lorentzian functions centered at the scaled B3LYP/6-311++G(d,p) calculated wavenumbers (bottom). Note that the calculated intensities correspond, in the simulated spectrum, to the areas below the Lorentzian functions and not to peak intensities.

$$E(2) = \Delta E_{ij} = q_i \frac{F_{ij}^2}{\varepsilon_j - \varepsilon_i} \quad (1)$$

where F_{ij}^2 is the Fock matrix element between i and j NBO orbitals, ε_j and ε_i are the energies of the acceptor and donor NBOs, and q_i is the occupancy of the donor orbital.

As it is shown in Table 2 and Figure 1, the most relevant NBO interactions, A, B and C, involve electron charge transfer from the lone electron pair (LP) of the nitrogen atoms to the carbonyl bonds π antibonding orbitals, and can be directly related with the mesomeric structures **II**, **III**, and **IV** presented in Figure 1. In the case of N1, the electron charge transfer is exclusive to the π^*(C2═O7) antibonding orbital, whereas N3 donates electronic charge to both π^*(C2═O7) and π^*(C4═O9) antibonding orbitals. As we could expect, due to the competition between the two interactions involving the N3 atom, the interaction energies for LP(N3) → π^*(C2═O7) (47.70 kcal mol^{-1}) and LP(N3) → π^*(C4═O9) (54.65 kcal mol^{-1}) orbital interactions are smaller than that corresponding to the LP(N1) → π^*(C2═O7) (57.88 kcal mol^{-1}) orbital interaction. Furthermore, as a whole, the electronic charge transferred from N1 and N3 atoms to the π^*(C2═O7) antibonding orbital is considerably higher than the one that results from the single interaction associated with the π^*(C4═O9) antibonding orbital, a result that is in agreement with the more negative π charge of O7 (−0.532 e) compared to O9 (−0.483 e). As seen, all these results are truly consistent with the conclusions that were extracted from the structural data presented before, in particular the relative lengths of the different C═O and C_{sp2}−N bonds (C2═O7 > C4═O9; C2−N1 < C4−N3 < C2−N3).

The other main NBO interactions (D-I) are correlated with other types of intramolecular interactions: (a) The NBO orbital interactions named as D, E, F, and G occur between the nonbonded electron pair (LP2; σ) of O7 and O9 oxygen atoms and the antibonding σ^* orbitals of the neighbor C−N bonds. This type of interaction represents the well-known electron back-donation effect involving carbonyl oxygen atoms[31−33] that explains, for example, the unusually long C−H bond length in aldehydes and derivatives of formic acid, and that reflects also in the uncommonly low ν(C−H) stretching vibrational frequency in these types of molecules. In 5-MH, these interactions also contribute to determine the relative lengths of the C2−N3, C4−N3, and C2−N1 bonds (1.412, 1.378, and 1.369 Å respectively): the stronger the back-donation from the donor carbonyl lone pair to the acceptor antibonding orbital of a given C_{sp2}−N ring-bond, the longer the bond. (b) The NBO orbital interactions designated H and I describe the electronic charge transfer from the second nonbonded electron pair (LP1; σ) of the oxygen atoms O7 and O9 to one Rydberg orbital of the corresponding carbonyl carbon atom. These interactions are associated with effects related to the carbonyl bond polarization, working specifically as moderators of the σ polarization of the carbonyl bonds to compensate the effects of the increased π polarization due to the interactions A, B, and C.

The analysis of the s−p composition of the hybrid NBO's of the ring carbon and nitrogen atoms (Table 3) allows us to explain why the internal angles of the ring are considerably larger when we have a nitrogen atom in the angle apex (C4−N3−C2 and C2−N1−C5) than when it is the carbon in the angle apex (N1−C2−N3, N3−C4−C5, and N1−C5−C4). As mentioned above, this observation suggests different *s-p* composition of the hybrid orbitals of the C and N atoms that are presented in the ring bonds. A smaller p contribution to the hybrid orbital correlates with larger angles,[34,35] so that the average p contribution to the hybrid orbitals used to establish the ring bonding NBOs by the nitrogen atoms N1 and N3 is smaller than the used by the carbon atoms C2, C4 and C5.

3.3. IR Spectrum of Matrix-Isolated 5-MH. The experimental infrared spectrum of monomeric 5-MH isolated in argon matrix (10 K) is presented in Figure 2, together with the B3LYP/6-311++G(d,p) calculated IR spectrum of the compound. The calculated normal modes were analyzed by means of their potential energy distributions (PED), which are shown together with the proposed assignments in Table 4. In general terms, the experimental and calculated spectra agree very well. The most prominent band in the spectrum, belonging to the antisymmetric carbonyl stretching vibration (ν(C═O)$_{as}$) is observed at 1768 cm^{-1} (calculated, 1776 cm^{-1}), while the band associated with the symmetric carbonyl stretching vibration (ν(C═O)$_s$) is observed at 1811 cm^{-1} (calculated at 1812 cm^{-1}). Similar to what has been reported for the parent hydantoin[17] and 1-MH,[18] the small band observed at 1753 cm^{-1} is probably due to the first overtone of the ring vibration whose fundamental appears at 782 cm^{-1} enhanced by Fermi resonance interaction with ν(C═O)$_{as}$. The out-of-plane C2═O7 and C4═O9 modes (γ(C═O)′ and γ(C═O)″, respectively) are observed at 756 and 729 cm^{-1}, in good agreement with the calculated data (747, 717 cm^{-1}). The higher frequency value for the γ(C═O)′ mode, compared to γ(C═O)″, reflects the greater rigidity of the NH−C2═O7−NH fragment in relation to out-of-plane deformation, compared to the NH−C4═O9−C(H)CH$_3$ fragment, as expected considering the presence of two NH/C═O interactions in the first and of only one in the second.

The NH vibrations appear as site-split bands, which is an indication of the sensitivity of this vibration to the matrix environment. The N1−H6 stretching vibration (ν(NH)′) gives rise to a doublet of bands at 3510 and 3499 cm^{-1}, while the N3−H8 stretching vibration (ν(NH)″) is observed as a triplet

DOI: 10.1021/acs.jpca.7b05030
J. Phys. Chem. A 2017, 121, 5267−5279

Table 4. Infrared Spectrum of Monomeric 5-MH in Argon Matrix (10 K) and DFT(B3LYP)/6-311G++(d,p) Calculated Infrared Spectrum and Potential Energy Distributions (PED)[a]

experimental (Ar matrix; 10 K)	calculated		
wavenumber[b]	wavenumber	I_{IR}[c]	PED[d] (%)
3510/3499	3501	54	ν(NH)′(100)
3491/3487/3481	3481	84	ν(NH)″ (100)
2990	3059	10	$\nu(CH_3)_{as}'$ (93)
2947	3046	17	$\nu(CH_3)_{as}''$ (93)
2920	2978	15	$\nu(CH_3)_s$ (99)
2888	2954	16	ν(CH) (87)
1811	1812	238	$\nu(C{=}O)_s$ (79)
1768/ ∼ 1753	1776	1024	$\nu(C{=}O)_{as}$ (76)
1459	1467	2	$\gamma(CH_3)_{as}'$ (87)
1454	1465	8	$\gamma(CH_3)_{as}''$ (85)
1403/1399	1395	32	δ(NH) ′(41) + $\delta(CH_3)_s$ (12) + δ(CH) (11)
1390	1383	43	$\delta(CH_3)_s$ (77)
1367	1360	102	ν(NH)′(15) + $\nu(C{=}O)'$ (11) + ν_4(ring) (11)
1341	1330	52	δ(NH)″(49) + ν_1(ring) (20)
1324/1317	1315	60	γ(CH) (43) + δ(NH)″(13) + $\gamma(C{-}CH_3)'$ (10)
1284	1267	84	δ(CH) (28) + ν_4(ring) (12) + δ(NH)′ (10)
1179	1166	67	δ(CH) (29) + ν_1(ring) (18) + ν_3(ring) (11) + δ_2(ring) (11)
1119	1106	7	$\delta(CH_3)_{as}''$ (23) + δ(CH) (13) + δ(NH)′ (12) + ν_4(ring) (11) + ν_2(ring) (10)
1088	1091	14	$\delta(CH_3)_{as}'$ (36) + ν(CC) (35) + $\gamma(C{-}CH_3)'$ (13)
1036	1027	25	$\delta(CH_3)_{as}''$ (20) + $\delta(CH_3)_{as}'$ (15) + ν(CC) (13)
982/978	972	26	ν_2(ring) (26) + ν_5(ring) (21) + ν_1(ring) (11)
943/940/937/936	931	10	$\delta(CH_3)_{as}'$ (26) + δ_2(ring) (21) + ν_4(ring) (14)+ ν_1(ring) (11)
782	793	10	ν_5(ring) (25) + $\delta(CH_3)_{as}'$ (14) + $\gamma(C{=}O)''$ (11)
756	747	14	$\gamma(C{=}O)'$ (87)
729	717	6	$\gamma(C{=}O)''$ (35)
664/662	653	12	δ_2(ring) (17) + $\gamma(C{=}O)''$ (16) + ν_3(ring) (15)
629/627	616	14	δ_1(ring) (49) + ν_5(ring) (16) + δ_2(ring) (10)
570/565	568	99	γ(NH)″ (64) + $\delta(C{=}O)'$ (16) + $\delta(C{=}O)''$ (12)
555/550	548	65	γ(NH)″ (38) + $\delta(C{=}O)'$ (20) + δ_2(ring) (14) + $\delta(C{=}O)''$ (13)
n.i.	433	16	$\gamma(C{-}CH_3)'$ (15) + τ_1(ring) (69) + γ(NH)′ (72)
n.i.	377	15	$\delta(C{=}O)'$ (31) + $\delta(C{=}O)''$ (26)
n.i.	347	67	γ(NH)′ (72) + $\gamma(C{-}CH_3)'$ (15) + $\delta(C{-}CH_3)$ (13)
n.i.	237	6	$\delta(C{-}CH_3)$ (56) + $\gamma(C{=}O)''$ (12) + $\gamma(C{-}CH_3)'$ (10)
n.i.	227	0.3	$\tau(CH_3\text{-ring})$ (96)
n.i.	130	0.4	τ_2(ring) (76) + τ_1(ring) (18)
n.i.	78	6	τ_1(ring) (69) + τ_2(ring) (23)

[a]See Table S2 for the definition of coordinates and Scheme 1 for atom numbering. Abreviations: s, symmetric; as, antisymmetric; ν, stretching; δ, in-plane bending; γ, out-of-plane bending; τ, torsion, n.i., not investigated. [b]Wavenumbers in cm^{-1}. [c]IR intensities in km mol^{-1}. [d]PED's lower than 10% not shown.

of bands at 3491, 3487, and 3481 cm^{-1}. The relative values of the frequencies of the two NH stretching vibrations correlate well with the lengths of the two bonds, the higher the frequency the shorter the N−H bond (the N1−H6 and N3−H8 bond lengths are predicted to be 1.007 and 1.010 Å, respectively; see Table S3).

The N1−H6 and N3−H8 in-plane bending vibrations (δ(NH)′ and δ(NH)″, respectively) are observed at 1403/1399 and 1341 cm^{-1} respectively, in good agreement with the theoretical predictions (1395 and 1330 cm^{-1}). The N3−H8 out-of-plane bending vibration (γ(NH)″) is observed as a site-split doublet with relatively high intensity at 570/565 cm^{-1} (according to the normal-mode analysis, the N3−H8 out-of-plane bending coordinate also contributes significantly to the doublet observed at 555/550 cm^{-1}), while the analogous vibration of the N1−H6 moiety (γ(NH)′) is predicted to occur at 347 cm^{-1}, i.e., below the spectral range available for investigation.

The band corresponding to the CH stretching vibration is observed at 2888 cm^{-1}, at a slightly lower frequency than the predicted one (2954 cm^{-1}), while the bending vibrations of this moiety are predicted and observed in the range between 1315 and 1165 cm^{-1}, in good general agreement with the theoretical predictions (see Table 4). The CH_3 vibrations are observed in their usual ranges and their assignment was straightforward (Table 4).

3.4. UV-Induced Photolysis of Matrix-Isolated 5-MH.

The matrix-isolated 5-MH monomers were subjected to a series of UV irradiations with different wavelengths. Narrowband irradiations in the wavelength range 230−222 nm led to spectral changes similar to those resulting from broadband irradiation performed with the Hg(Xe) lamp (λ > 220 nm), but in a smaller extension. Upon 20 h of broadband irradiation, half of the compound was consumed, with new bands being observed in the spectrum which belong to the generated photoproducts.

DOI: 10.1021/acs.jpca.7b05030
J. Phys. Chem. A 2017, 121, 5267−5279

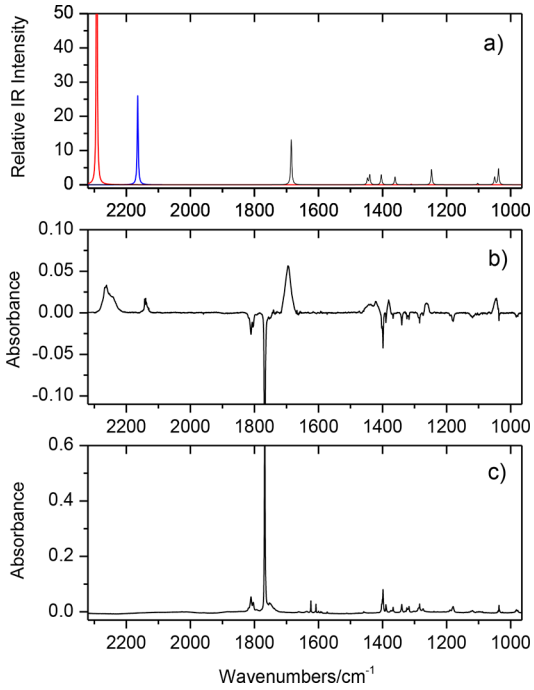

Figure 3. (a) B3LYP/6-311++G(d,p) calculated (scaled) infrared spectra (2320−965 cm^{-1} region) for CO (blue), isocyanic acid (red) and methanimine (black); (b) infrared difference spectrum (irradiated matrix; 20 h; broadband) *minus* (as deposited spectrum); (c) as deposited spectrum of 5-MH in argon matrix.

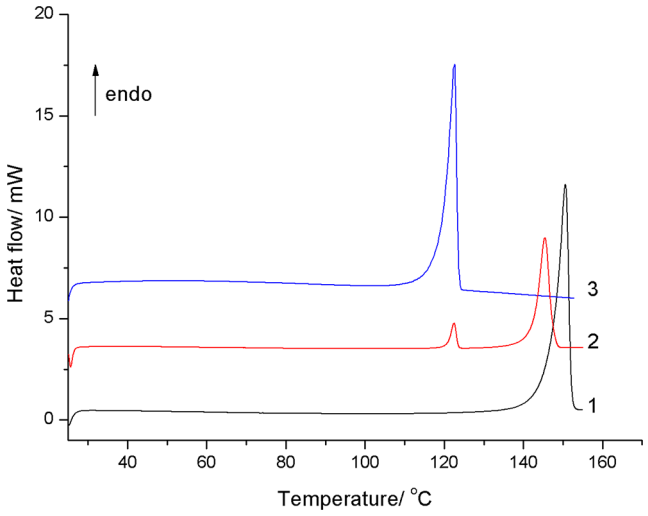

Figure 4. 5-MH DSC heating curves from 25 to 155 °C, β = 10 °C min^{-1}. (1) Original 5-MH commercial substance (polymorph **I**), mass = 1.76 mg. (2) 5-MH sample obtained by recrystallization of the melted original sample (polymorph **II**), mass = 1.19 mg. (3) 5-MH sample obtained by recrystallization of the melted original sample as polymorph **III**, mass = 1.97 mg.

Figure 3 shows selected regions of a difference spectrum, showing the most characteristic bands of the photoproducts resulting from UV irradiation of matrix-isolated 5-MH. The spectrum was obtained by subtracting the spectrum of the initially deposited matrix of 5-MH from that obtained after broadband UV irradiation for 20 h. Identification of the photoproducts is straightforward: (a) isocyanic acid (OCNH) is in the origin of the multiplet band with maxima at 2268, 2262, 2252, and 2241 cm^{-1}, which is assigned the NCO asymmetric stretching vibration, and also to the weak bands observed at 749, 573, and 1327 cm^{-1}, due to the δ_{HNC}, the δ_{NCO}, and the $\delta_{HNC} + \delta_{NCO}$ modes, respectively,[36] (b) the bands in the 2145−2129 cm^{-1} region are due to carbon monoxide (CO),[37] and (c) the remaining bands can be assigned to ethanimine (C_2H_5N), the most intense band belonging to CN stretching vibration of this photoproduct being observed as a broad band with maximum at ca. 1690 cm^{-1} (calculated, 1685 cm^{-1}); other bands of ethanimine were observed at 2975, 2938, 1437, 1422, 1381, 1266, 1217, 1046, and 880 cm^{-1}, which were predicted at 3007, 2960, 1447/1440, 1404, 1361, 1247, 1049/1039 and 904 cm^{-1}, respectively. Note that the photoproducts must be interacting to each other in the matrix cage where they are generated, so that their vibrational signatures show signals of this condition, i.e., band broadening and splitting, and small band shifts compared to the frequencies of the same compounds well-isolated in an argon matrix.[36,37] Nevertheless, the identification of the three photoproducts is unequivocal.

The observed photoproducts indicate that, upon UV irradiation, 5-MH undergoes photofragmentation through a single pathway, which might be proposed to be identical to that observed previously for the parent hydantoin[17] and which was also found to take place in 1-MH.[18] Such a pattern of reactivity then emerges as a general photoreaction of the hydantoin moiety.

3.5. Thermal Analysis Investigation of 5-MH. The purchased neat crystalline sample of 5-MH, from now on named as polymorph **I**, was investigated in relation to its thermal properties. According to the performed DSC studies, the melting of the 5-MH polymorph **I** occurs at T_{fus} = (147.2 ± 0.6) °C, with an enthalpy of fusion of $\Delta_{fus}H$ = (17.2 ± 0.2) kJ mol^{-1} (curve 1, Figure 4).

As also proven by polarized light thermal microscopy (Figure 5, part 1) no further events were observed during the heating process of polymorph I, besides the described melting of the sample.

From heating/cooling cycles, performed on the molten compound by DSC and PLTM, three new polymorphs (**II**, **III**, **IV**) of 5-MH could be identified. Melting of polymorph **II** occurs at T_{fus} = (143.0 ± 0.4) °C (Figure 4, curve 2) and polymorph **III** (Figure 4, curve 3), which was the most frequently obtained in DSC melt crystallization experiments, melts at T_{fus} = (120.1 ± 0.8) °C with enthalpy $\Delta_{fus}H$ = (13.1 ± 0.1) kJ mol^{-1}. Polymorph **IV** was only observed in PLTM experiments, melting at ca. 94−96 °C (part 4, Figure 5). A scanning rate of 10 °C min^{-1} was used in most of the experiments. Other scanning rates were tried, 2, 5, and 25 °C min^{-1}, leading to no additional conclusions.

PLTM allowed obtaining a deeper insight on the melt crystallization processes. In the PLTM experiments, it was possible to observe that in general, when cooling the molten compound, the liquid starts to crystallize at ca. 40−44 °C as a solid material, whose Raman spectrum could be recorded in the PLTM generated sample and it is shown in Figure S1. The crystal growth is interrupted at temperatures lower than 30 °C, once the motion of the molecules is obstructed by the higher viscosity of the liquid at lower temperatures. As the sample is heated again, at temperatures higher than 32−36 °C, the crystals start to grow again and the initially formed crystals convert to polymorph **III** in a very slow and gradual solid−solid transition that starts at 60 °C and lasts for ca. 40 °C (third to seventh images of part 2, Figure 5). Polymorph **III** eventually melts or this event is followed by a fast solid−solid phase

DOI: 10.1021/acs.jpca.7b05030
J. Phys. Chem. A 2017, 121, 5267−5279

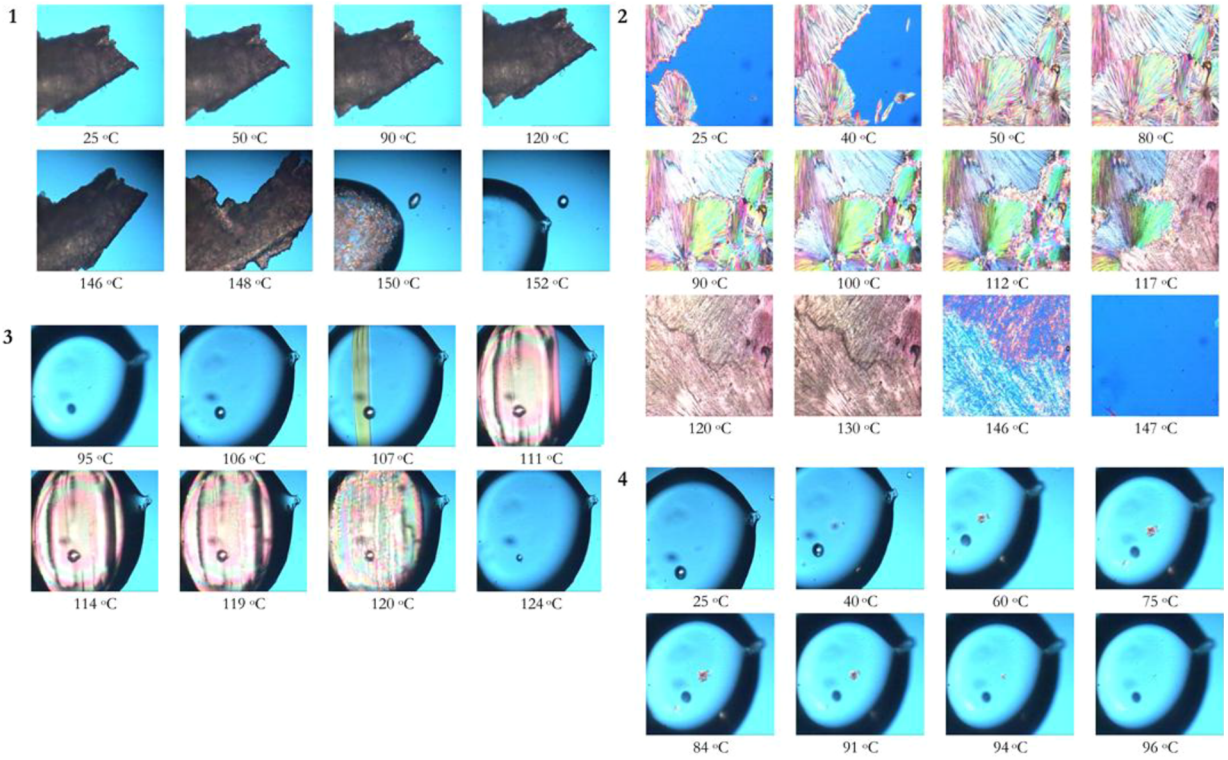

Figure 5. Polarized light thermal microscopy images collected in 5-MH heating process from 25 to 155 °C, β = 10 °C min^{-1}, and amplification 200×. (1) Melting of the commercial 5-MH substance (polymorph **I**); (2) heating of the 5-MH sample obtained by recrystallization of the melted compound, showing conversions of the initial solid material into **III** and **III** into **II**, and the melting of this later; (3) 5-MH sample obtained by recrystallization of the melted compound with direct formation of polymorph **III** and melting of this polymorph; (4) 5-MH sample obtained by recrystallization of the melted compound, with formation of polymorph **IV**, and melting of polymorph **IV** (for a magnified picture see Figure S2).

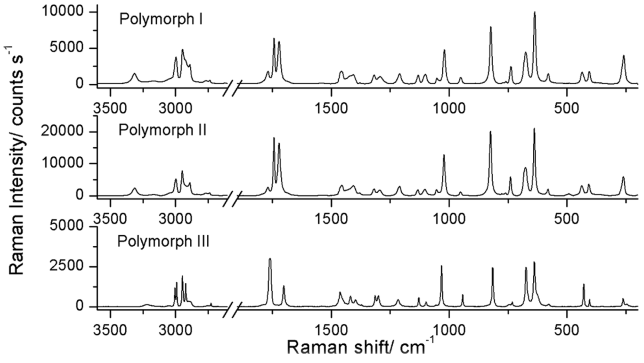

Figure 6. Raman spectra of polymorphs **I**–**III** of 5-MH.

transition that gives rise to polymorph **II** (eighth and ninth images of part 2, Figure 5): conversion of this first crystalline material into **II** takes place in two steps, through two solid–solid phase transitions.

Though polymorphs **II** and **III** could be obtained directly upon cooling/heating the melt (e.g., polymorph **III** can be sometimes obtained in the heating run, at ca. 107 °C; see Figure 5, part 3, following melt cooling to 25 °C), most frequently the result is the production of the already related metastable material that originates—first polymorph **III** and eventually polymorph **II**—via solid–solid transitions. This behavior was not detected in the DSC studies, either because we were not able to generate it in such conditions, or because the solid–solid transition is imperceptible in this technique, as the range of temperature where it exists is too broad.

Formation of the polymorph **II** upon heating the cooled melt occurs either directly (very seldom) or from polymorph **III**. This latter might also result directly from the recrystallization of the melt, as already mentioned above, or from transformation of the initially formed material. The solid–solid transition converting **III** into **II** occurs at ca. 115–118 °C (Figure 5, part 2). An additional crystalline phase, polymorph **IV**, was also detected, obtained by the cooling of the molten compound, as tiny crystals that melt at ca. 94–96 °C, as shown in Figure 5, part 4.

5-MH was recrystallized in different types of solvents: aprotic polar solvents (THF and acetone), protic and polar solvents (water, methanol and ethanol) and nonpolar solvents (dichloromethane and 1,4-dioxane) were used in the recrystallization process. THF solutions yield a heterogeneous mixture of polymorphs **I**, **II**, and **III**, and ethanol solutions produced a mixture of polymorphs **I** and **III**, probed by Raman microscopy. All the other solutions only originated polymorph **I**.

Polymorphs **I**, **II**, and **III** of 5-MH were investigated by single crystal Raman spectroscopy. In this type of experiment, the spectral intensity patterns can be significantly affected by the orientation of the crystal relative to the polarization direction of the laser beam. Hence, in order to be sure that the spectrum corresponded to the named polymorph, after the collection of the Raman spectra, all the crystals analyzed by this technique were submitted to heating processes in PLTM experiments to confirm each polymorphic thermal behavior. In all cases the effects of the intermolecular interactions are clearly visible when the spectra are compared to the vibrational data obtained for the monomeric molecule (either calculated or

DOI: 10.1021/acs.jpca.7b05030
J. Phys. Chem. A 2017, 121, 5267–5279

Table 5. Raman Bands (cm^{-1}) of the Observed Polymorphs of 5-MH at 25°C, with Proposed Assignments[a]

freq			
polymorph **I**	polymorph **II**	polymorph **III**	assignment
3315	3312	3310	ν(NH)′
3315	3312	3310	ν(NH) ″
2996	2997	2997	$\nu(CH_3)_{as}$″
2946	2948	2945	$\nu(CH_3)_{as}$′
2923	2890	2893	$\nu(CH_3)_s$
2889	2766/2738	2766/2737	ν(CH)
1768/1742	1768/1743	1768/1753	$\nu(C{=}O)_s$
1721	1721	1701	$\nu(C{=}O)_{as}$
1543	1546/1536	1535	δ(NH)″
1460	1461	1461	$\gamma(CH_3)_{as}$′
1455	1455	1446	$\gamma(CH_3)_{as}$″
1424	1436/1419	1428	δ(NH) ′
1405	1406	1401	$\delta(CH_3)_s$
1377	1379	1378	ν_4(ring)
1317	1318	1318	γ(CH)
1293/1291	1294	1307/1300	δ(CH)
1209	1210	1206	ν_1(ring)
1130	1132	1138	$\delta(CH_3)_{as}$″
1110	1102	1106	ν(CC)
1051	1053	1056	$\delta(CH_3)_{as}$′
1019	1021	1033	ν_2(ring)
950	951	950	δ_2(ring)
823	824	819	ν_5(ring)
759	776/760	767	$\gamma(C{=}O)$′
738	739	736	$\gamma(C{=}O)$″
675	676	671	ν_3(ring)
637	638	638	δ_1(ring)
579	580	599	γ(NH)″
	492	491	$\delta(C{=}O)$″
435	437	442/432	$\gamma(C{-}CH_3)$′
404	407	419/407	$\delta(C{=}O)$′
258	260	255	$\delta(C{-}CH_3)$
177	178	179	$\tau(CH_3$-ring)
157/144	146	142	τ_2(ring)
82	89	82	τ_1(ring)

[a]See Scheme 1 for atom numbering; assignments correspond to approximate descriptions of the vibrations chosen as the main coordinate contributing to the vibration and are based on the PED's obtained for the isolated monomer (see Table 4). Abbreviations: γ, rocking; ν, stretching; δ, bending; τ, torsion; s, symmetric; as, antisymmetric.

matrix isolation IR spectra; see also Figure S3, in the Supporting Information, for calculated Raman spectrum of the isolated 5-MH molecule). For example, all solid phase spectra show a large frequency downshift of the NH stretching vibrations compared with that of the matrix-isolated compound. The bands corresponding to the NH stretching modes appear in the different polymorphs at about 3315 and 3140 cm^{-1}, while in the spectrum of the monomeric 5-MH these modes give rise to bands appearing at 3510/3499 and 3491/3487/3481 cm^{-1} (see Figures 2 and 6 and Tables 4 and 5). The proposed simplified assignments for the Raman spectra of the crystalline phases of 5-MH are given in Table 5.

As shown in Figure 6, the Raman spectra of polymorphs **I** and **II** are very similar, except in relation to relative band intensities (e.g., the ratio between the carbonyl intensities to the bands due to the N−H stretching vibrations, which is higher for the case of polymorph **II**) and the extra band at 492 cm^{-1} in the spectrum of polymorph **II**. This indicates that the orientation of the 5-MH molecules in both crystals should be very similar. Nevertheless, the different identity of the two polymorphs was doubtlessly confirmed by DSC and PLTM (exhibiting their characteristic behaviors; see above) and also by powder X-ray diffraction (see section 3.6). On the other hand, the Raman spectrum of polymorph **III** are clearly distinctive from those of polymorphs **I** and **II**, in particular in the C=O stretching region, with the first two polymorphs having a single band at 1768 cm^{-1} and a doublet at 1742/1721 cm^{-1}

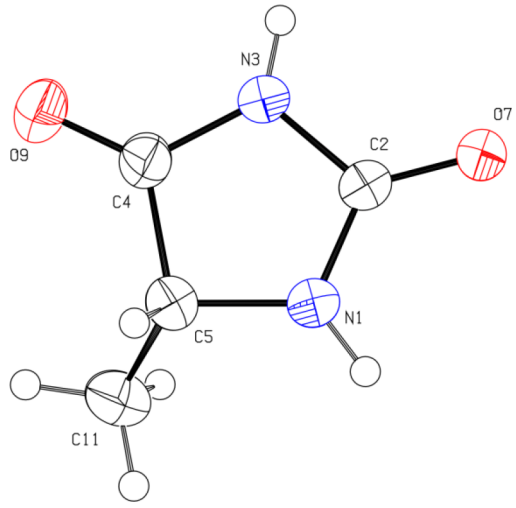

Figure 7. ORTEP plot of the molecule (polymorph **III**) showing the atom numbering scheme. Anisotropic displacement ellipsoids are drawn at the 50% probability level.

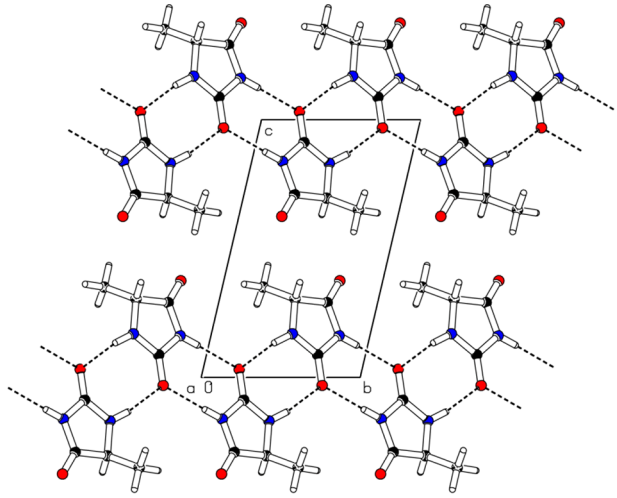

Figure 8. Projection of the crystal structure along the *a*-axis showing the hydrogen bonding pattern.

Table 6. Distances and Angles of Intermolecular Hydrogen Bonds of 5MH (Polymorph III)[a]

	D-H (Å)	H···A (Å)	D···A (Å)	D-H···A (deg)
N3−H8···O7$^{(i)}$	0.84(3)	2.00(3)	2.836(2)	177(3)
N1−H6···O7$^{(ii)}$	0.88(3)	2.01(3)	2.881(2)	171(2)
C5−H10···O9$^{(iii)}$	0.98	2.57	3.348(3)	136.2

[a]Symmetry codes: (i) 1 − *x*, 2 − *y*, −*z*; (ii) 2 − *x*, 1 − *y*, −*z*; (iii) 1 + *x*, *y*, *z*.

DOI: 10.1021/acs.jpca.7b05030
J. Phys. Chem. A 2017, 121, 5267−5279

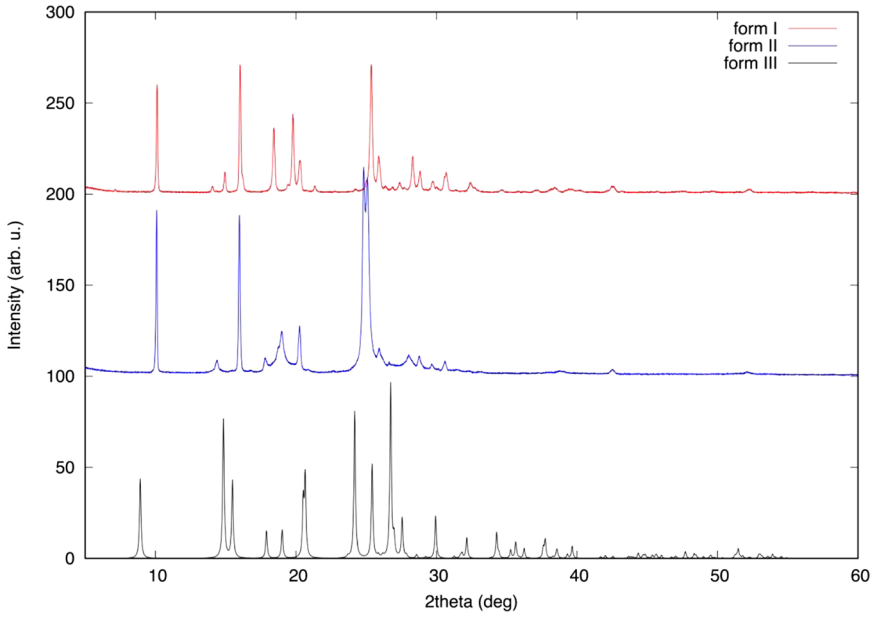

Figure 9. Powder XRD diffractograms of polymorphs **I**, **II** (experimental), and **III** (calculated from single-crystal data). The data was measured with Cu Kα radiation. The patterns were shifted along the vertical axis for clarity.

(assignable to the symmetric and antisymmetric carbonyl stretching vibrations), and polymorph **III** giving rise to two bands at 1752 and 1701 cm^{-1}. These differences suggest a significant dissimilarity in the H-bond network of polymorph **III** compared to those of polymorphs **I** and **II**.

3.6. X-ray Diffraction (XRD) Studies. The structure of polymorph **III** was determined by XRD analysis performed on a small single crystal obtained by recrystallization from ethanol. The ORTEP plot of the molecule in polymorph **III** is shown in Figure 7. Anisotropic displacement ellipsoids are drawn at the 50% probability level.

This polymorph crystallizes in the triclinic $P-1$ space group with two molecules per unit cell related by the inversion center. Molecule geometry determined from XRD is in good agreement with that determined by the DFT calculations. Valence angles are accurately reproduced, while experimental bond lengths are systematically slightly shorter due to the well-known effect of thermal smearing. After correction of such effect using a rigid-body model for libration motion of the molecule derived from a fit of the experimental anisotropic thermal ellipsoids, the bond-lengths are also very close to the DFT calculated values. The most notable exception is the significant increase of the C2═O7 bond observed in the crystal compared to that of the calculated for the isolated molecule [1.228(2) uncorrected, 1.232 corrected vs 1.208 Å DFT]. This can be ascribed to the participation of the O7 as acceptor in strong hydrogen bonds. In fact, in the crystal the molecules are packed in layers (Figure 8). In each layer the molecules are joined in infinite chains running parallel to the [1−10] axis through a head to tail pattern of hydrogen bonding involving the C═O and N−H groups. The O7 bond is an acceptor of two N−H bonds, the O9 atom is not involved in strong hydrogen bonds, but a short intramolecular distance [3.348(3) Å] exists between the O9 atom and one H atom of the methyl group of a neighbor molecule that could be classified as a weak hydrogen bond (Table 6). In addition, $C_g\cdots C_g$ interactions between the π electron clouds of the rings probably play also an important role in stabilizing the crystal structure.

Unfortunately, polymorphs **I**, **II**, and **IV** could not be obtained in single-crystal form. However, powder XRD patterns were collected for polymorphs **I** and **II**. The diffractograms are depicted in Figure 9, compared to the calculated powder diffraction for polymorph **III**. Cleary the three polymorphs correspond to different crystalline structures.

4. CONCLUSION

5-Methylhydantoin was investigated as an isolated molecule and also in the neat solid phases. As isolated species, 5-MH was studied by matrix isolation infrared spectroscopy and theoretical calculations carried out at the DFT(B3LYP)/6-311++G(d,p) theory level. In the neat solid phases, the compound was investigated by DSC, PLTM, XRD, and Raman spectroscopy.

The IR spectrum of 5-MH monomeric form isolated in a low-temperature argon matrix was obtained and interpreted. Assignments were made for the experimentally observed IR bands, which received support from theoretical vibrational data, including the results of the performed normal coordinates' analysis.

The structure of the molecule was characterized thoroughly using the theoretically obtained data. This included the evaluation of the details of its electronic structure by using the NBO method, namely the assessment of the specific characteristics of the σ and π electronic systems of the molecule, and the stabilizing orbital interactions.

Photochemical experiments were performed on the matrix-isolated compound, revealing that upon UV irradiation the 5-MH molecule photofragments through a single reaction pathway, yielding isocyanic acid, ethanimine and carbon monoxide, thus following a pattern already observed before for the parent hydantoin and 1-methylhydantoin molecules.

The thermal study of the neat solid compound allowed identification of four different polymorphs. The crystal structure of one of the polymorphs (polymorph **III**), for which it was possible to grow up suitable crystals, was determined by X-ray diffraction. Two of the additional

DOI: 10.1021/acs.jpca.7b05030
J. Phys. Chem. A 2017, 121, 5267−5279

polymorphs (**I** and **II**) were characterized by powder XRD. Polymorphs **I**, **II**, and **III** were also characterized by Raman spectroscopy.

On the whole, the performed investigations provided a comprehensive structural, spectroscopic and thermodynamic study of the targeted compound.

■ ASSOCIATED CONTENT

Supporting Information

The Supporting Information is available free of charge via the Internet at The Supporting Information is available free of charge on the ACS Publications website at DOI: 10.1021/acs.jpca.7b05030.

Figure S1, with the Raman spectrum of the solid material obtained in the PLTM experiments upon cooling the melted compound; Figure S2, with a magnified picture of the recrystallization of the melted compound, with formation and subsequent melting of polymorph IV; Figure S3, with the B3LYP/6-311++G(d,p) calculated Raman spectrum for the isolated molecule of 5-MH; Table S1, with the summary of X-ray data collection and refinement parameters (for polymorph III); Table S2, with the definition of the internal coordinates used in the normal modes' analysis; and Table S3, with the optimized geometry of 5-methylhydantoin calculated at the B3LYP/6-311++G(d,p) level of theory. (PDF)

■ AUTHOR INFORMATION

Corresponding Authors

*(B.A.N.) E-mail: ban@qui.uc.pt. Telephone:+351-913061106. Fax: +351-239827704.

*(G.O.I.) E-mail: g.ogruc@iku.edu.tr. Telephone: +902124984319. Fax:+90 212 4658310.

ORCID

G. O. Ildiz: 0000-0002-7827-5050

Notes

The authors declare no competing financial interest.

■ ACKNOWLEDGMENTS

This investigation has been performed within the Project PTDC/QEQ-QFI/3284/2014 − POCI-01-0145-FEDER-016617, funded by the Portuguese "Fundação para a Ciência e a Tecnologia" (FCT) and FEDER/COMPETE 2020-EU. The Coimbra Chemistry Centre (CQC) is supported by FCT, through Project UI0313/QUI/2013, also cofunded by FEDER/COMPETE 2020-EU. CFisUC is funded by FCT through Project UID/FIS/04564/2016. Access to instruments from the TAIL-UC facility funded under QREN-Mais Centro Project ICT_2009_02_012_1890 is gratefully acknowledged.

■ REFERENCES

(1) Sarges, R.; Schnur, R. C.; Belletire, J. L.; Peterson, M. J. Spirohydantoin Aldose Reductase Inhibitors. *J. Med. Chem.* **1988**, *31*, 230−243.

(2) Park, H. S.; Choi, H. J.; Shin, H. S.; Lee, S. K.; Park, M. S. Synthesis and Characterization of Novel Hydantoins as Potential COX-2 Inhibitors: 1,5-Diarylhydantoins. *Bull. Korean Chem. Soc.* **2007**, *28*, 751−757.

(3) Cruz-Cabeza, A. J.; Schwalbe, C. H. Observed and Predicted Hydrogen Bond Motifs in Crystal Structures of Hydantoins, Dihydrouracils and Uracils. *New J. Chem.* **2012**, *36*, 1347−1354.

(4) Yu, F.; Schwalbe, C. H.; Watkin, D. J. Hydantoin and Hydrogen Bonding Patterns in Hydantoin Derrivatives. *Acta Crystallogr., Sect. C: Cryst. Struct. Commun.* **2004**, *60*, o714−o717.

(5) Amharar, Y.; Petit, S.; Sanselme, M.; Cartigny, Y.; Petit, M. N.; Coquerel, G. Crystal Structures, Dehydration Mechanism, and Chiral Discrimination in the Solid State of a Hydantion Derivative. *Cryst. Growth Des.* **2011**, *11*, 2453−2462.

(6) Coquerel, G.; Petit, M. N.; Robert, F. Structure of (+)-(*S*)-5-Phenyl-5-ethylhydantoin. *Acta Crystallogr., Sect. C: Cryst. Struct. Commun.* **1993**, *49*, 824−825.

(7) Coquerel, G.; Petit, M. N. Recognition of Enantiomers through Morphology of Single Crystals; Application to Some 5-Alkyl-5-aryl-hydantoin Derivatives. *J. Cryst. Growth* **1993**, *130*, 173−180.

(8) Ananda Kumar, C. S.; Kavitha, C. V.; Vinaya, K.; Prasad, S. B. B.; Thimmegowda, N. R.; Chandrappa, S.; Raghavan, S. C.; Rangappa, K. S. Synthesis and *in Vitro* Cytotoxic Evaluation of Novel Diazaspiro Bicyclo Hydantoin Derivatives in Human Leukemia Cells: A SAR Study. *Invest. New Drugs* **2009**, *27*, 327−337.

(9) Kavitha, C. V.; Nambiar, M.; Ananda Kumar, C. S.; Choudhary, B.; Muniyappa, K.; Rangappa, K. S.; Raghavan, S. C. Novel Derivatives of Spirohydantoin Induce Growth Inhibition Followed by Apoptosis in Leukemia Cells. *Biochem. Pharmacol.* **2009**, *77*, 348−363.

(10) Yang, K.; Tang, Y.; Iczkowski, K. A. Phenyl-methylene Hydantoins Alter CD44-Specific Ligand Binding of Benign and Malignant Prostate Cells and Suppress CD44 Isoform Expression. *Am. J. Transl. Res.* **2010**, *2*, 88−94.

(11) Comber, R. N.; Reynolds, R. C.; Friedrich, J. D.; Manguikian, R. A.; Buckheit, R. W.; Truss, J. W.; Shannon, W. M.; Secrist, J. A. 5,5-Disubstituted Hydantoins: Syntheses and Anti-HIV Activity. *J. Med. Chem.* **1992**, *35*, 3567−3572.

(12) Konnert, L.; Reneaud, B.; de Figueiredo, R. M.; Campagne, J. M.; Martinez, J.; Colacino, E.; et al. Mechanochemical Preparation of Hydantoins from Amino Esters: Application to the Synthesis of the Antiepileptic Drug Phenytoin. *J. Org. Chem.* **2014**, *79*, 10132−10142.

(13) Fujisaki, F.; Shoji, K.; Shimodouzono, M.; Kashige, N.; Miake, F.; Sumoto, K. Antibacterial Activity of 5-Dialkylaminomethylhydantoins and Related Compounds. *Chem. Pharm. Bull.* **2010**, *58*, 1123−1126.

(14) Marton, J.; Enisz, J.; Hosztafi, S.; Tímar, T. Preparation and Fungicidal Activity of 5-Substituted Hydantoins and Their 2-Thio Analogs. *J. Agric. Food Chem.* **1993**, *41*, 148−152.

(15) Nakajima, M.; Itoi, K.; Takamatsu, Y.; Kinoshita, T.; Okazaki, T.; Kawakubo, K.; Shindo, M.; Honma, T.; Tohjigamori, M.; Haneishi, T. Hydantocidin: a New Compound with Herbicidal Activity from *Streptomyces Hygroscopicus*. *J. Antibiot.* **1991**, *44*, 293−300.

(16) Ildiz, G. O.; Boz, I.; Unsalan, O. FTIR Spectroscopic and Quantum Chemical Studies on Hydantoin. *Opt. Spectrosc.* **2012**, *112*, 665−670.

(17) Ildiz, G. O.; Nunes, M. C.; Fausto, R. Matrix Isolation Infrared Spectra and Photo-chemistry of Hydantoin. *J. Phys. Chem. A* **2013**, *117*, 726−734.

(18) Nogueira, B. A.; Ildiz, G. O.; Canotilho, J.; Eusébio, M. E. S.; Fausto, R. Molecular Structure, Infrared Spectra, Photochemistry and Thermal Properties of 1-Methylhydantoin. *J. Phys. Chem. A* **2014**, *118*, 5994−6008.

(19) Niku-Paavola, M. L.; Laitila, A.; Mattila-Sandholm, T.; Haikara, A. New Types of Antimicrobial Compounds Produced by Lactobacillus Plantarum. *J. Appl. Microbiol.* **1999**, *86*, 29−35.

(20) Sabbah, R.; An, X. W.; Chickos, J. S.; Planas Leitão, M. L. P.; Roux, M. V.; Torres, L. A. Reference Materials for Calorimetry and Differential Thermal Analysis. *Thermochim. Acta* **1999**, *331*, 93−204.

(21) Bruker *APEX2, SAINT and SADABS*; Bruker AXS Inc.: Madison, WI, 2014).

(22) Sheldrick, G. SHELXT - Integrated Space-Group and Crystal-Structure Determination. *Acta Crystallogr., Sect. A: Found. Adv.* **2015**, *71*, 3−8.

(23) Sheldrick, G. Crystal Structure Refinement with SHELXL. *Acta Crystallogr., Sect. C: Struct. Chem.* **2015**, *71*, 3−8.

DOI: 10.1021/acs.jpca.7b05030
J. Phys. Chem. A 2017, 121, 5267−5279

(24) Spek, A. Structure Validation in Chemical Crystallography. *Acta Crystallogr., Sect. D: Biol. Crystallogr.* **2009**, *65*, 148−155.
(25) Frisch, M. J.; Trucks, G. W.; Schlegel, H. B.; Scuseria, G. E.; Robb, M. A.; Cheeseman, J. R.; Scalmani, G.; Barone, V.; Mennucci, B.; Petersson, G. A.; et al. *Gaussian 09*, Revision D.01, Gaussian, Inc.: Wallingford CT. 2009.
(26) Becke, A. D. Density-Functional Exchange-Energy Approximation with Correct Asymptotic Behavior. *Phys. Rev. A: At., Mol., Opt. Phys.* **1988**, *38*, 3098−3100.
(27) Lee, C. T.; Yang, W. T.; Parr, R. G. Development of the Colle-salvati Corelation Energy Formula into a Functional of Electron Density. *Phys. Rev. B: Condens. Matter Mater. Phys.* **1988**, *37*, 785−789.
(28) McLean, A. D.; Chandler, G. S. Contracted Gaussian-basis Sets for Molecular Calculations. 1. 2nd row atoms, Z = 11−18. *J. Chem. Phys.* **1980**, *72*, 5639−5648.
(29) Lapinski, L.; Nowak, M. J. *BALGA Suit of Computer Programs for PED Calculations*; Institute of Physics Polish Academy of Sciences: Warsaw.
(30) Fox, M. A.; Whitesell, J. K. *Organische Chemie: Grundlagen, Mechanismen, Bioorganische Anwendungen*; Springer: Berlin, 1995.
(31) Fausto, R.; Batista de Carvalho, L. A. E.; Teixeira-Dias, J. J. C.; Ramos, M. N. s-cis and s-trans Conformers of Formic, Thioformic and Dithioformic Acids. An Ab Initio Study. *J. Chem. Soc., Faraday Trans. 2* **1989**, *85*, 1945−1962.
(32) McKean, D. C. Individual CH Bond Strengths in Simple Organic Compounds: Effects of Conformation and Substitution. *Chem. Soc. Rev.* **1978**, *7*, 399−422.
(33) Castiglioni, C.; Gussoni, M.; Zerbi, G. Intramolecular Electrical and Dynamical Interactions in Formaldehyde: A Discussion Based on Infrared Intensity Data. *J. Chem. Phys.* **1985**, *82*, 3534−3541.
(34) Fausto, R. Bonding in Carbonyl and Thiocarbonyl Compounds: An Ab Initio Charge Density Study of H_2C = X and HC(=X)YH (X,Y= O or S). *J. Mol. Struct.: THEOCHEM* **1994**, *315*, 123−136.
(35) Wiberg, K. B.; Laidig, K. E. Rotational Barriers Adjacent to Carbonyl Groups 3. Amide Resonance and the C-O Barrier in Acids and Esters. *J. Am. Chem. Soc.* **1987**, *109*, 5935−5943.
(36) Teles, J. H.; Maier, G.; Andes Hess, B. A., Jr.; Schaad, L. J.; Winnewisser, M.; Winnewisser, B. P. The CHNO Isomers. *Chem. Ber.* **1989**, *122*, 753−766.
(37) Abe, H.; Takeo, H.; Yamada, K. M. T. Infrared Spectroscopy of CO Trapped in an Argon Matrix Revisited. *Chem. Phys. Lett.* **1999**, *311*, 153−158.

DOI: 10.1021/acs.jpca.7b05030
J. Phys. Chem. A 2017, 121, 5267−5279